Effect of film thickness and temperature on condensation and momentum accommodation at the liquid–vapor methane interphase in contact with a quartz substrate

Gbocho Gilles Soboh, Quy-Dong To, Irina Graur, Frédéric Topin, Vincent Monchiet, Céline Léonard

Effect of film thickness and temperature on condensation and momentum accommodation at the liquid-vapor methane interphase in contact with a quartz substrate

Gbocho Gilles Soboh[a], Quy-Dong To[a,*], Irina Graur[b], Frédéric Topin[b], Vincent Monchiet[a], Céline Léonard[a]

[a] *Univ Gustave Eiffel, Univ Paris Est Creteil, CNRS UMR 8208, MSME, F-77454 Marne-la-Vallée, France*
[b] *Université Aix Marseille CNRS, UMR 7343, IUSTI, 13453, Marseille, France*

Abstract

In this paper, we used the Molecular Dynamics method to simulate the equilibrium vapor-liquid methane in contact with a solid quartz substrate and study the condensation process and momentum exchange at the atomic level. A large potential cutoff radius is used to determine the vapor and liquid densities at good accuracy. By tracking the motions of fluid molecules exchanged between the vapor and liquid phases and carrying out statistical analysis of residence time, penetration depth and especially velocity correlation, the mass and especially, the velocity accommodation coefficients can be determined at the same time. The latter is based on the assumption that the reflected events take place over a short time, near the interface and thus atoms velocities are correlated while the condensation/evaporation events are not. The calculated coefficients are sensitive to the film thickness due to the presence of the quartz substrate and the layering effects. As temperature increases, atoms condense less and reflect more and the reflection is more dif-

*Corresponding author
Email address: quy-dong.to@univ-eiffel.fr (Quy-Dong To)

fusive due to increasing collision rate. Near the critical temperature, both the condensation and momentum accommodation coefficients vary significantly.

Keywords: Evaporation condensation coefficient, accommodation coefficient, molecular dynamics, boundary conditions, vapor liquid interphase

1. Introduction

Liquid vapor phase change processes are ubiquitous phenomena in nature and have numerous industrial applications including power generation, water processing and environmental control, etc. Thus, understanding those phenomena is very important in both theoretical and technological aspects. While the characters of liquid and vapor in distinct bulk phase can be well described by transport equations at the continuum scale like Navier Stokes and Fourier equations etc., the correct description of heat and mass exchanges at the interface and their evolution require the implementation of molecular level approaches. In this case, Molecular Dynamics (MD) is a powerful method that can provide access to the atomic picture of the process and this information can be used to construct macro and mesosopic models. This is the main motivation of the present work.

In literature, the condensation and evaporation coefficients [1, 2] were introduced to characterize the mass exchange between the two phases. Simple definition of these coefficients can be done as following. The condensation coefficient is the ratio between the condensing flux and the total incoming flux of vapor into the liquid phase. The evaporation coefficient is the ratio between the spontaneous evaporation flux and the total outgoing flux of liquid into the vapor phase. Under equilibrium conditions, when the evaporation and condensations fluxes are equal between them, these coefficients are equal while when evaporation or condensation flux occurs in non-equilibrium conditions, they could be different. However, in most applications, those two coefficients are usually assumed to be identical.

First notable theoretical estimates of the evaporation and condensation mass flux based on principles of the kinetic theory and involving the evaporation/condensation coefficients have been derived, such as the Hertz-Knudsen [1, 3] and the Schrage expressions [4, 5]. Later, the improved expressions for the evaporation and condensation fluxes were derived from the moment method by Anisimov [6] and then Ytrehus [7]. However, all these expressions involved unknown evaporation/condensation coefficients. Large amount of the experimental data on these coefficients can be found in the literature. Unfortunately all these data are very scattered: for example the measured values of the evaporation coefficients of water differ, according to various sources, in four orders of magnitude [8]. This fact can be explained by many reasons as difficulties of such kind of measurements, validity of models used for extraction of the data on the evaporation/condensation coefficient from the measured quantities etc.

An another way to identify these coefficients is to simulated the evaporation-condensation process by the Molecular Dynamics method. Different approaches based on MD simulations have been proposed. Most of them are based on the travelling distance of molecules from one phase to the other [9, 10], and on the residence time of the molecules [11] or on the energy [12]. Physically speaking, condensing vapor molecules have tendency to penetrate deeper and stay longer in the liquid phase. Various studies have been done to investigate cases of large molecules [13, 14], the dependency of curvature [15] and the verification of theoretical formula by MD simulations [16, 17, 18]. However, the liquid and vapor phases are usually considered as the bulk phase, which is not true for the early stage of the condensation process where both the very thin liquid film and the substrate can interplay. While momentum and energy accommodation coefficients play significant role in determination of velocity slip and temperature jump at the interface [19], they are neglected in the studies of vapor-liquid interphases.

The objective of the present work is to use MD simulations to determine more

accurately the scattering behavior of vapor at the interphase by determining the evaporation/condensation coefficients as well as the tangential momentum accommodation coefficient. The latter is largely used in a scattering model that serves as boundary conditions at a gas solid surface interface for kinetic and continuum transport equations at rarefied conditions, i.e. the ratio between the molecular mean free path and the characteristic dimension of a problem is large. To this end, the velocity, displacement and residence time of atoms are tracked and collected as data, which are then analyzed in the case of the methane vapor condensing on quartz substrate. Specifically, the tangential momentum accommodation coefficients are determined via correlation analysis [20, 21]. Moreover, we also examine the case of thin liquid films of methane on the solid substrate, find that the film thickness and the substrate nature have impacts on those accommodation coefficients. The consideration of common geomaterials like methane and quartz also provides useful results for future applications. For examples, methane is a shale gas and shale is mainly a mixture of clay materials such as kaolinite and quartz or silica [22, 23, 24]. In addition, silica can also be a suitable material for methane storage [25]. Moreover, methane can efficiently be described by the united atom model [26] which simplifies the molecular dynamics simulation. The details of the present work will be presented in the following.

2. Theoretical background

2.1. Kinetic boundary conditions of Boltzmann equation

As it was underlined in Introduction, during the condensation process a vapor is in its non-equilibrium state and the continuum approach fails to describe accurately the condensation phenomenon. In this case, the Boltzmann equation is used to simulate the evolution of the distribution function $f(\boldsymbol{c}, \boldsymbol{x})$ of velocity $\boldsymbol{c}$ in every location $\boldsymbol{x}$ of the gas phase. It must be completed by boundary conditions at the interface with materials of different natures like

solid wall or liquid phase. Let us assume the interface, denoted in the following by w, is parallel to the z plane and define the input distribution f^{in} and the output one f^{out} as follows

$$f^{in}(\boldsymbol{c}) = \begin{cases} 0, & \forall c_z > 0 \\ f(\boldsymbol{c}), & \forall c_z < 0 \end{cases} \qquad \text{and} \qquad f^{out}(\boldsymbol{c}) = \begin{cases} f(\boldsymbol{c}), & \forall c_z > 0 \\ 0, & \forall c_z < 0 \end{cases} \tag{1}$$

so that

$$f(\boldsymbol{c}) = f^{out}(\boldsymbol{c}) + f^{in}(\boldsymbol{c}). \tag{2}$$

A general kinetic boundary condition (KBC) links the input distribution f^{in} and the output one f^{out}

$$|c_z| f^{out}(\boldsymbol{c}) = \int_{c'_z<0} B(\boldsymbol{c}|\boldsymbol{c}')|c'_z| f^{in}(\boldsymbol{c}')d\boldsymbol{c}', \quad c_z > 0, \tag{3}$$

where $B(\boldsymbol{c}|\boldsymbol{c}')$ is the scattering kernel. In equilibrium, we must have

$$f^{in}(\boldsymbol{c}) = \frac{n_w}{2}\mathcal{M}(\boldsymbol{c}) \quad \forall c_z < 0, \quad f^{out}(\boldsymbol{c}) = \frac{n_w}{2}\mathcal{M}(\boldsymbol{c}) \quad \forall c_z > 0 \tag{4}$$

with $\mathcal{M}(\boldsymbol{c})$ being the Maxwellian

$$\mathcal{M}(\boldsymbol{c}) = \left(\frac{m}{2\pi k_B T_w}\right)^{3/2} e^{-\frac{m|\boldsymbol{c}|^2}{2k_B T_w}}, \tag{5}$$

where m is the mass of the fluid molecule and n_w is the gas number density at the interface at temperature T_w and k_B is the Boltzmann constant. In the case of liquid-vapor phase change at the interface

$$n_w = n^v_{sat}(T_w), \tag{6}$$

where n^v_{sat} is the saturated vapor number density at the interface temperature T_w.

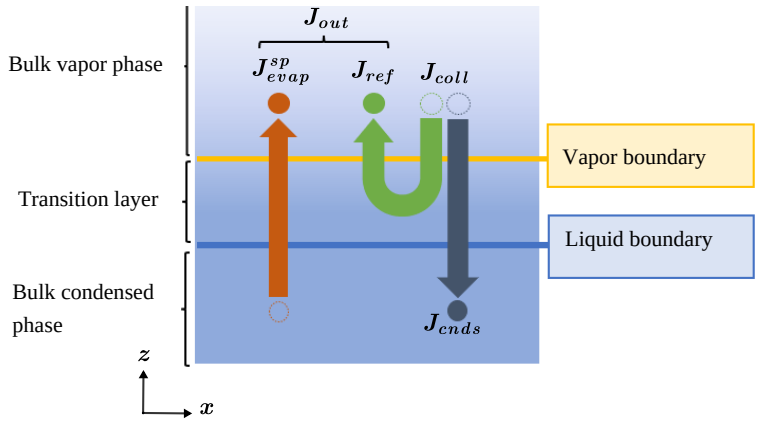

Figure 1: Sketch of the liquid-gas interphase and the fluxes. The positions of the liquid and vapor boundaries as well as the thickness of the transition layer are discussed in Section 3.1.

As shown in Fig. 1, a kinetic boundary model can be constructed by assuming that the flux of the molecules can be decomposed into evaporation (evap), condensation (cnds), and reflection (ref) processes. For example, we can write

$$f^{out} = f^{evap} + f^{ref/out}, \quad J^{out} = J^{evap} + J^{ref}, \quad c_z > 0 \tag{7}$$

and

$$f^{in} = f^{cnds} + f^{ref/in}, \quad J^{in} = J^{cnds} + J^{ref}, \quad c_z < 0 \tag{8}$$

with

$$J^a = \int |c_z| f^a(\boldsymbol{c}) d\boldsymbol{c}, \tag{9}$$

where superscript a stands for any of notations "in", "out", "evap", "cnds", or "ref/in" and, "ref/out". Due to the identity $J^{ref/out} = J^{ref/in}$, we use J^{ref} to denote both $J^{ref/out}$ and $J^{ref/in}$. Well-known boundary conditions

[27] can be used

$$f^{out}(\boldsymbol{c}) = \alpha_e n_{sat}^v \mathcal{M}(\boldsymbol{c}) + (1-\alpha_c)[\alpha n_w \mathcal{M}(\boldsymbol{c}) + (1-\alpha) f^{in}(\boldsymbol{c}^s)], \quad c_z > 0, \tag{10}$$

with the number density of molecules, n_w, calculated from classical impermeability conditions

$$n_w = \sqrt{\frac{2\pi m}{k_B T_w}} \int_{c_z<0} |c_z| f^{in} d\boldsymbol{c}, \tag{11}$$

and $\boldsymbol{c}^s$ is the mirror velocity of $\boldsymbol{c}$ with respect to the interface normal to $\widehat{\boldsymbol{i}}_z$

$$\boldsymbol{c}^s = \boldsymbol{c} - 2c_z \widehat{\boldsymbol{i}}_z. \tag{12}$$

We can thus identify $f^{evap} = \alpha_e n_{sat} \mathcal{M}(\boldsymbol{c})$ as the evaporation term and $f^{ref/out} = (1-\alpha_c)[\alpha n_w \mathcal{M}(\boldsymbol{c}) + (1-\alpha) f^{in}(\boldsymbol{c}^s)]$ as the outgoing reflection term. The latter is composed of a diffusive part $\alpha n_w \mathcal{M}(\boldsymbol{c})$ and a specular part $(1-\alpha) f^{in}(\boldsymbol{c}^s)$. In addition, the relation $f^{ref/in} = (1-\alpha) f^{in}(\boldsymbol{c})$ is assumed for the incoming reflection term as in the Maxwell reflection model. The coefficients α_c and α_e are respectively the condensation and evaporation coefficients and α is the momentum/energy accommodation coefficient as in the classical Maxwell diffuse-specular kernel [28]. In equilibrium, the two coefficients evaporation and condensation are equal, $\alpha_c = \alpha_e$. For practical reason, this equality is also used for non equilibrium case, assuming that the condition is not far from equilibrium.

The boundary conditions can be more conveniently analyzed using the normalized probability distribution function associated with the flux crossing the interface, defined as

$$p^a(\boldsymbol{c}) = \frac{|c_z| f^a(\boldsymbol{c})}{\int |c_z| f^a(\boldsymbol{c}) d\boldsymbol{c}}. \tag{13}$$

Assuming $\alpha_c = \alpha_e$, we rewrite the evaporation and reflection terms using the normalized flux distribution as

$$p^{out}(\boldsymbol{c}) = \alpha_c p^{evap}(\boldsymbol{c}) + (1 - \alpha_c) p^{ref/out}(\boldsymbol{c}), \tag{14}$$

where the evaporation term reads

$$p^{evap}(\boldsymbol{c}) = \sqrt{\frac{2\pi m}{k_B T_w}} |c_z| \mathcal{M}(\boldsymbol{c}). \tag{15}$$

It is possible to relate $p^{ref/out}(\boldsymbol{c})$ to $p^{in}(\boldsymbol{c})$, in a similar way as by Eq. (3) using a scattering kernel $B(\boldsymbol{c}|\boldsymbol{c}')$ as

$$p^{ref/out}(\boldsymbol{c}) = \int_{c'_z<0} B(\boldsymbol{c}|\boldsymbol{c}') p^{in}(\boldsymbol{c}') d\boldsymbol{c}'. \tag{16}$$

In this case expression for $p^{ref/out}$ becomes

$$p^{ref/out}(\boldsymbol{c}) = \alpha p^{diff}(\boldsymbol{c}) + (1 - \alpha) p^{spec}(\boldsymbol{c}) \tag{17}$$

with

$$p^{diff}(\boldsymbol{c}) = \sqrt{\frac{2\pi m}{k_B T_w}} |c_z| \mathcal{M}(\boldsymbol{c}), \qquad p^{spec}(\boldsymbol{c}) = p^{in}(\boldsymbol{c}^s). \tag{18}$$

It is known that the Maxwell model has different shortcomings, for example, the meaning of the coefficient α is not clearly defined. It can be accommodation of tangential momentum or of energy. In addition, it exhibits discontinuity in velocity space and in reality, no molecule has an ideal specular reflection. An alternative way is the implementation of the Cercignani-Lampis (CL) kernel which involves two accommodation parameters α_t and α_n, for accommodation of the tangential momentum and normal energy, respectively. Expressions for both Maxwell and Cergignani-Lampis kernels and the relation for the correlation between the velocities are given in Appendix

A.

In any case, for a fluid in equilibrium, we have the following remarks:

- The tangential velocity of a reflected molecule (associated to distribution $p^{ref/out}$) is correlated with its incoming tangential velocity (associated to distribution p^{in}) with correlation coefficient $(1-\alpha)$.
- The velocity of an evaporated molecule (associated to distribution p^{evap}) is uncorrelated with its incoming velocityassociated to distribution $p^{ref/out}$), resulting in a zero correlation coefficient.
- The correlation coefficient between the incoming tangential velocity (associated to distribution p^{in}) and the outgoing tangential velocity (associated to distribution p^{out}) is $(1-\alpha)(1-\alpha_c)$.

These properties are valid for both Maxwell and Cergignani-Lampis kernels. In addition, to the statistical property, the condensed gas molecules tend to penetrate deep into the liquid phase and stay longer in it. Thus using the above observations, if we can distinguish the condensed molecules and reflected molecules, the condensation and the accommodation coefficients can be determined by correlation techniques.

We noted that in literature there are mainly two numerical methods of identifying the evaporation/condensation and tangential momentum accommodation coefficients characterizing interaction between a gas and a surface (solid or liquid). The first one is to beam atoms at fixed angles and velocities and measure the change of tangential velocities. However, due to the complex scattering behavior, the obtained coefficient is not constant and depends on the beaming angles [29]. It is also difficult to employ this method in the interphase problem as there are many atoms moving constantly across the liquid and vapor phases. The second method is to generate collision data with random angles and incoming velocities, e.g those issued from equilibrium state, then construct statistical scattering models and their parameters, including

correlation coefficients, to fit the data [30, 31, 20, 21]. The latter approach which is statistically robust and suitable for the interphase problem, will be adopted in this work.

The presented above methods of identification of the coefficients characterizing gas surface (solid or liquid) interaction are consistent with the kinetic boundary conditions, Eq. (10) as in Refs. [9, 10]. Some literature works proposed that those coefficients depend on the molecular kinetic energy [12, 14]. This corresponds to more sophisticate statistical modelling of the boundary conditions and will not be pursued further.

2.2. Molecular Dynamics simulations

The models are composed of quartz (SiO_2) substrate and methane (CH_4) molecules with periodic boundary conditions in x, y directions. The geometric parameters of SiO_2 crystal unit cell are as follows: $a = b = 4.9137$Å, $c = 5.4047$Å, $\alpha = \beta = 90^0$, $\gamma = 120^0$. The solid rectangular substrate volume is $8a \times 9\sqrt{3}b/2 \times 4c$ and in all our simulations, it is composed of 864 Si atoms and 1728 O atoms (see Fig. 2). The dimensions of the simulation box along x, y are equal to the corresponding dimensions of the silica substrate, i.e. $L_x = 8a = 39.3096$ Å, $L_y = 9\sqrt{3}b/2 = 38.2985$ Å while the dimension L_z is larger and varied so that we can fill the space with methane molecules.

The Burckingham (BKS) force field [32]

$$V_{ij}^{BKS} = C\frac{q_i q_j}{r_{ij}} + A_{ij}\exp\left(-b_{ij}r_{ij}\right) - \frac{c_{ij}}{r_{ij}^6} \tag{19}$$

is used to describe the interaction between the quartz atoms, Si and O. In previous equation r_{ij} is the distance between atoms i and j of charges q_i and q_j. The constants A_{ij}, b_{ij}, c_{ij} are the parameters of BKS potential, C is the energy conversion constant for the Coulombic term. The values of those constants are given in Table 1.

The Lennard-Jones (LJ) potential

$$V_{ij}^{LJ} = 4\epsilon_{ij}\left[\left(\frac{\sigma_{ij}}{r_{ij}}\right)^{12} - \left(\frac{\sigma_{ij}}{r_{ij}}\right)^{6}\right] \tag{20}$$

is used to describe the interaction between CH_4 molecules via TraPPE force field [26] within the unified atom model. The values of the parameters of LJ potential, ϵ_{ij} and σ_{ij}, namely the depth of potential well (or dispersion energy) and the distance at which the particle-particle potential energy V_{ij}^{LJ} is zero (often referred to as size of the particle), are given in Table 2.

Results in Ref. [26] show that this model is very well suited to describe both liquid and gas phases of methane in the temperature range of the present work, i.e. 110-170 K. Moreover, the lowest energetic vibrational mode of CH_4 is the bending deformation mode associated with an equivalent temperature of 1879 K. The temperature of the simulations will not exceed 170 K, and Boltzmann's statistics indicate that less than 0.002% of the molecules would be vibrationally excited at 170 K. The interactions between a CH_4 molecule and Si or O of the solid quartz are given via Lorentz–Berthelot mixing rule from CLAYFF force field [33]. The chemisorption process of CH_4 on quartz is supposed to be totally negligible.

The cutoff distance for force computation is $r_{cut} = 5.09\sigma_{CH_4} = 19$ Å, where σ_{CH_4} is the diameter of the methane molecule, and is less than half the shortest edge of the simulation box [34]. The reason to choose a value r_{cut} much larger than the usual value $r_{cut} = 2.5\sigma_{CH_4}$ in most MD simulations is that cutting too short the attractive tail of the LJ potential can significantly affect the liquid vapor coexistence curve. In other words, choosing large r_{cut} allows producing saturated densities of the same order as experiments. The quartz substrate is composed of one fixed lower layer and two upper layers maintained at temperature T_w by NVT thermostat. The other z boundary of the simulation box is an elastic reflected wall. A suitable quantity of CH_4 molecules is placed in the middle of the simulation box so that after

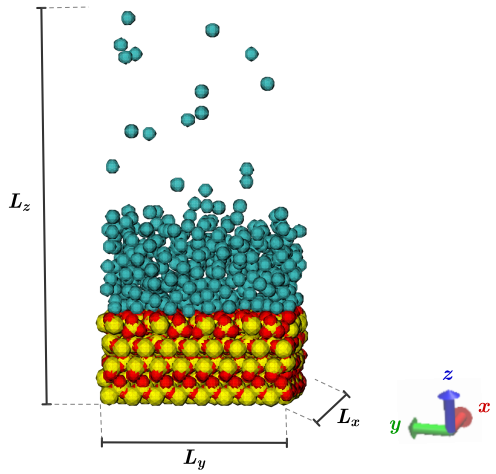

Figure 2: Snapshot of Molecular Dynamics system. Color code: blue for methane molecules (CH_4), red for oxygen atoms (O) and yellow for silicon atoms (Si).

equilibration process at T_w, CH_4 is accumulated into a liquid film on the quartz surface and diluted in the remaining space. The choice of temperature T_w is also important to guarantee that the two phases coexist and the gas phase is sufficiently dilute. In simulations, T_w is varied from 110K to 170K, which is above the triple point $T_{tp} = 90$K and below the critical point $T_c = 190$K[35]. In reduced LJ units, we have $T^* = k_B T_w/\epsilon_{CH_4} = 0.7432$ for 110K and $T^* = 1.14$ for 170K.

The open source MD code LAMMPS [36] is used for all the simulations. Additional tools are developed to track atom motions and output atom values when they cross the control plane. The latter is placed at distance δ from the liquid-vapor interface. Specifically, we are interested in the following quantities:

- the incoming velocity $\boldsymbol{c}'$ and the outgoing velocity $\boldsymbol{c}$
- the penetration depth d and the residence time τ between the incoming and outgoing events.

Due to the small gas density, 4×10^6 time steps of 0.0005 ps are required

Table 1: Parameters of BKS force field for quartz, Eq. (19).

	A_{ij}[eV]	b_{ij} [Å^{-1}]	c_{ij} [eV Å^6]	q_i[e]
O-O	1388.7730	2.7600	175.00	$q_O = -1.2$
Si-O	18003.7572	4.87318	133.5381	$q_{Si} = +2.4$

Table 2: Parameters of LJ potentials, Eq. (20).

	σ_{ij}[Å]	ϵ_{ij}/k_B [K]
CH_4-CH_4	3.7300	148.10
CH_4-Si	1.8650	0
CH_4-O	3.4480	107.60

to reach the equilibrium state and other 10^8 steps for outputting the data. Finally, we analyze the data distributions and construct the statistical based models for the liquid-vapor interface.

3. Results and discussion

3.1. Number density profile, saturated vapor number density and position of interface

Figures 3 and 4 show how the fluid number density varies with the coordinate z for different film thicknesses, which depend on the number of methane molecules N. If the liquid film of methane is sufficiently thick, we can observe a structuring effect near the quartz wall: the density is high and fluctuates strongly. Each peak corresponds to a layer of fluid molecules. Far from the solid wall, the fluid is more homogeneous and fluctuation is attenuated. Then, the number density decreases gradually in the transition zone and is quasi constant in the gaseous phase. For the case of 4 methane molecules, we only find one peak as the molecules only form one fluid layer. As the temperature increases, the interphase zone thickness is dilated (around 10 Å at 110K vs 20 Å at 170K). This could affect the mass and momentum exchanges between the liquid and vapor phases.

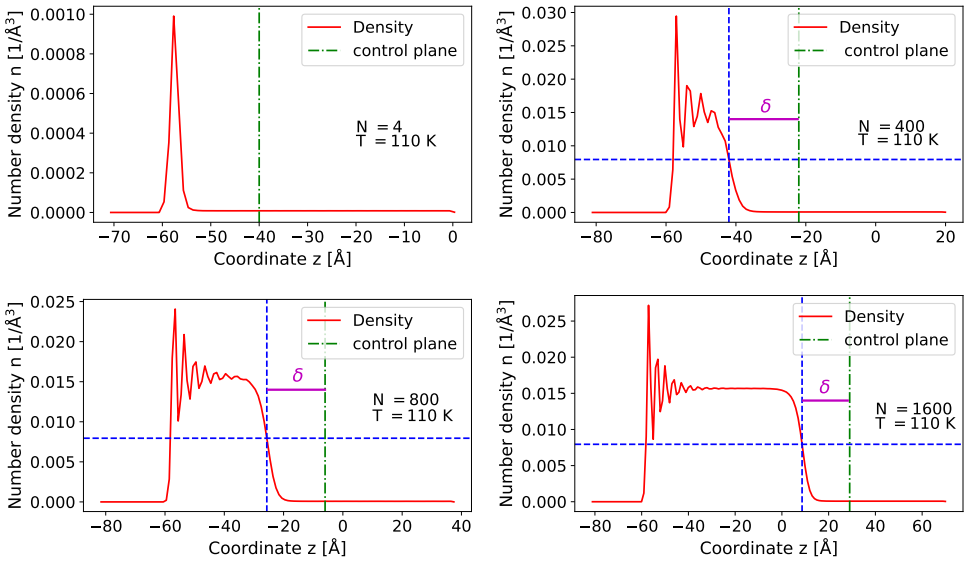

Figure 3: Number density of the fluid across the system at $T = 110$K and for different values of the methane molecules: (a) $N = 4$, (b) $N = 400$, (c) $N = 800$, (d) $N = 1600$. The leftmost part of each profile corresponds to the silica wall and has zero fluid number density. The rightmost part corresponds to the small but non vanishing gas number density. The vertical blue line corresponds to the liquid-gas interface, and the vertical green line to the control plane.

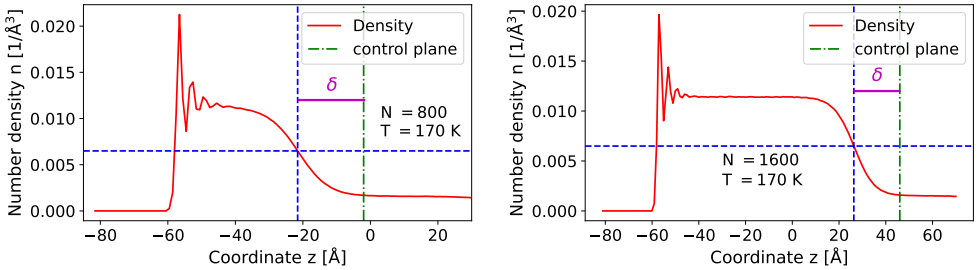

Figure 4: Number density of the fluid across the system at $T = 170$K and for different values of the methane molecules: (a) $N = 800$, (b) $N = 1600$. The leftmost part of the profile corresponds to the silica wall and has zero fluid number density. The rightmost part corresponds to the small but non vanishing gas number density. The vertical blue line corresponds to the liquid-gas interface, and the vertical green line to the control plane.

The value of saturated vapor number density n_{sat}^{v} can be obtained by fitting first the number density in the vapor phase with function

$$n(z) = a - b \tanh\left(2\frac{(z-c)}{d}\right), \tag{21}$$

where a, b, c and d are the fitting parameters. In addition, c is the location of interface and d is the interface thickness [37, 38]. Then, by looking for the limit value as

$$n_{sat}^{v} = \lim_{z\to\infty} n(z) = a - b. \tag{22}$$

In the case of large bulk liquid and gas phases, $a = \frac{1}{2}(n_{sat}^{v} + n_{sat}^{liq})$ and $b = \frac{1}{2}(n_{sat}^{liq} - n_{sat}^{v})$.

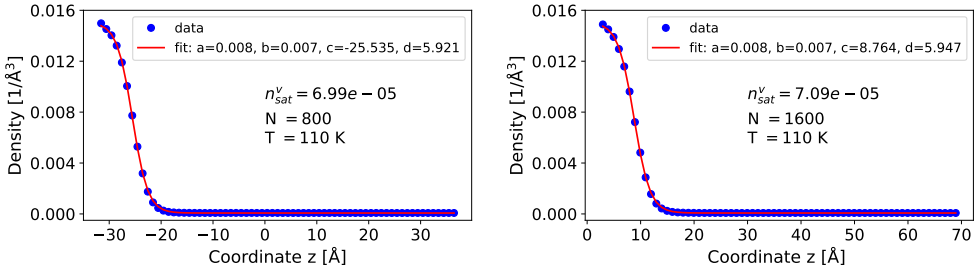

Figure 5: Saturated gas number density along direction z obtained from the numerical simulations (blue circles) and the fit according to Eq. (21) (red line).

At 110K, the saturated vapor number density is found to be $n_{sat}^{v} \simeq 0.07 \times 10^{-3}$ Å^{-3} which corresponds to reduced vapor number density $n_{sat}^{v*} = n_{sat}^{v}\sigma_{CH_4}^{3} = 0.0036$ at reduced temperature $T^* = 0.7432$ (see Figure 5). This value is lower than the MD results obtained by Liang *et al.* [11] $n_{sat}^{v*} = 0.0063$ at $T^* = 0.745$ using $r_{cut} = 3.2\sigma_{Ar}$ for argon, but in excellent agreement with LJ fluid simulations, $n_{sat}^{v*} = 0.0036$, using much larger r_{cut}, by Errington[39][1]

[1]Data available at https://www.nist.gov/mml/csd/chemical-informatics-research-group/sat-tmmc-liquid-vapor-coexistence-properties-cut

and 0.0033 by Stephan *et al.* [40]. It is also of the same order as $n_{sat}^{v*} = 0.0031$ from experimental data and equation of state (EOS) for methane [35], see also Appendix B for more details. At 170K, $T^* = 1.14864$, the value of saturated vapor number density from simulations is even closer to the literature value $n_{sat}^{v*} = 0.076$ which is identical to the value 0.076 obtained from EOS. In Ref. [39], the liquid–vapor phase equilibrium is directly determined using the transition matrix Monte Carlo (MC) simulation. In another recent work [40], the database composed of MC and MD simulations of the same equilibrium, found in literature, is examined and analytical formula that best fit the results are proposed.

The molecular mean free path λ of methane vapor is estimated from the vapor number density n and the LJ diameter of methane σ_{CH_4} as

$$\lambda = \frac{1}{\sqrt{2} n \pi \sigma_{CH_4}^2}. \tag{23}$$

The mean free path of methane vapor in saturated state is calculated from

$$\lambda = \frac{\sigma_{CH_4}}{\sqrt{2} \pi n_{sat}^{v*}} \tag{24}$$

and it is of order $\lambda = 62\sigma_{CH_4} = 231$ Å at 110K and $\lambda = 2.95\sigma_{CH_4} = 11$ Å at 170K. We note that at 170K, which is close to the critical temperature, the vapor phase is no longer dilute since the mean free path is of the same order as the cutoff distance of van der Waals forces.

Due to the transition zone, it is hard to determine the boundary between the liquid and vapor phases, i.e. the interface position. In the literature, there is no unique method to solve this problem. Moreover, the impact of the wall and the layering liquid structure, formed at the early stage of condensation, can pose additional difficulties. In this paper, we propose to locate the interface at the position where the fluid number density equals the average number

density of saturated vapor and saturated liquid

$$n_{int} = \frac{1}{2}(n_{sat}^{v} + n_{sat}^{liq}). \tag{25}$$

So defined interface position corresponds to the z coordinate value which equals to c in the fitting expression of the number density profile given by Eq. (21). This interface position (see vertical blue line on Figures 3 and 4) is thus also used to compute the nominal thickness of the liquid film condensed on silica.

When the liquid film is sufficiently thick, the wall is expected to have less impact on the exchange of molecules at the liquid-vapor interface and the transition zone is more dominant. As a results, it is important to define the limit of the liquid phase in the transition zone and the position of the control plane. The latter is used to determine the condensation and accommodation coefficients, or more generally the kinetic boundary conditions which represent probabilities of collision between a gas molecule and a liquid, and then the probability of condensation or reflection. The control plane is placed in the gaseous phase and at a certain distance δ from the interface position. The value of δ needs to be small when compare to the mean free path λ and the control plane must be sufficiently far from the liquid phase. This is due to the fact that we construct KBCs (Eq. (3)) associated with the evaporation/condensation and tangential momentum accommodation coefficients for the gaseous phase where the Boltzmann equation is valid. It is chosen so that gas molecule velocities are affected by the liquid only when crossing the control plane, in this case $\delta = 20$ Å (see Figures 3 and slightly larger than $r_{cut} = 19$ Å. In previous works, e.g Ref. [11, 15], this distance is also equal to $\delta = r_{cut}$. As the present work adopts a larger r_{cut} to obtain good saturated densities, δ value is thus consequently larger. Other works, e.g Refs. [41, 42, 43], chose to use δ as function of temperature and of the transition layer thickness which will result different evaporation/condensation coefficients. In our opinion, this consideration is also working as there is no

restriction, in terms of modelling, on where to apply the KBCs and those coefficients are expected to be associated with the KBCs position.

3.2. Residence time and penetration depth distributions

To study the condensation process, after each vapor molecule crosses the control plane towards the liquid phase, we track its motion to find how far and how long a molecule travels before reemerging at the control plane again. We assume that the incident flux can be decomposed into a reflected flux and a condensation flux, see Eq. (8). A reflected molecule is expected to be associated to a short residence time and a short penetration depth while a condensed molecule is expected to penetrate farther into the liquid phase and stay longer in it. We shall examine the Residence Time Distribution (RTD) and the Penetration Depth Distribution (PDD), and separate data associated to both types of fluxes (condensation and reflected) for further considerations. As above, we vary the number of methane molecules N in the model to study the influence of the liquid film thickness.

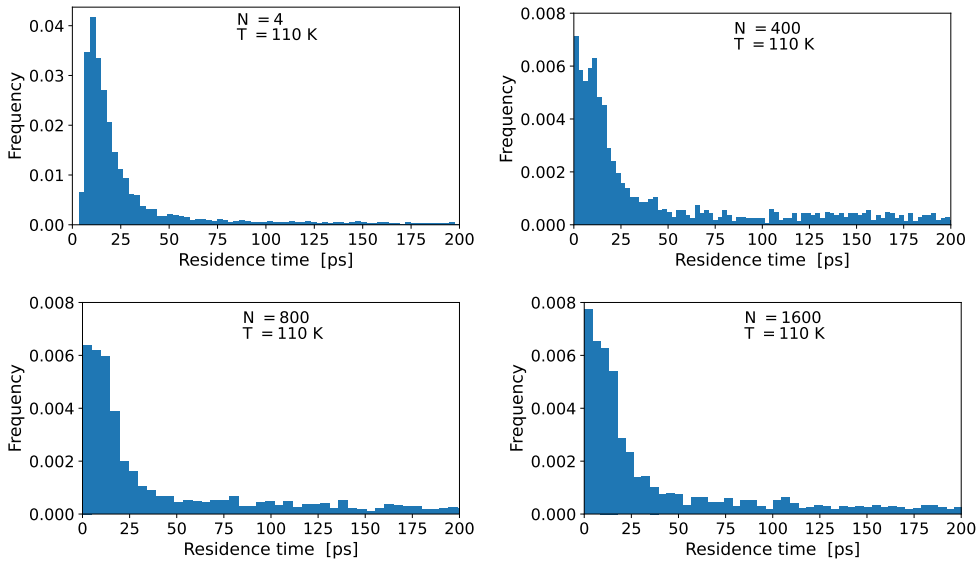

Figure 6: Residence time distributions at 110K.

From the histograms of the residence time τ at 110K (see Figure 6), we find that a large number of molecules has short residence time. The residence time probability decreases sharply from 0 to 40-50 ps and then decays slowly afterwards, ending by a long plateau. As a result, the residence time is clearly divided into two types of populations associated to two distinct regimes, a short residence time (shorter than 40 ps) and a long residence time (longer than 40 ps). For the case $N = 4$ molecules, the collisions occur mostly between the gas and the solid wall. The gas molecules are expected to travel the distance of order 2δ before reemerging at the control plane. As a result, a peak at 10-12 ps is visible in the distribution, which can be attributed to reflected molecules, given that the mean thermal speed equals 3.8 Å/ps and $2\delta = 40$ Å. We also observe that a large portion of the gas molecules is adsorbed and stays much longer than the peak value. For thicker liquid films, in addition to collisions with the bulk liquid at distance δ, the collisions can also occur in the gaseous phase at different distances from the control plane due to the presence of molecules in this area, showing a continuous distribution starting from 0 ps.

In the logarithmic time scale in Fig. 7, we find that the tail of the residence time distribution can be represented by a straight line, corresponding to an exponential distribution in long time regimes, i.e $\tau \sim e^{-\tau/\tau_r}$ at large τ, where τ_r is the relaxation time. From Figures 6 and 7, it is clear that the exponential regime tends to start for shorter residence times and to decrease with a faster rate (steeper slope in log scale) for higher temperatures, meaning a shorter relaxation time τ_r. For system composed of 800 molecules, although penetration depth data cloud starts to scatter at 20 Å and 25 ps (rather than 40 ps from RTD as discussed previously), we find that most molecules with residence times longer than 1000 ps come from the adsorbed liquid layers near the wall. This suggests that the main contribution of the exponential regime comes from molecules adsorbed near the silica wall. As the residence time can be considered as the sum of diffusion times in the gas

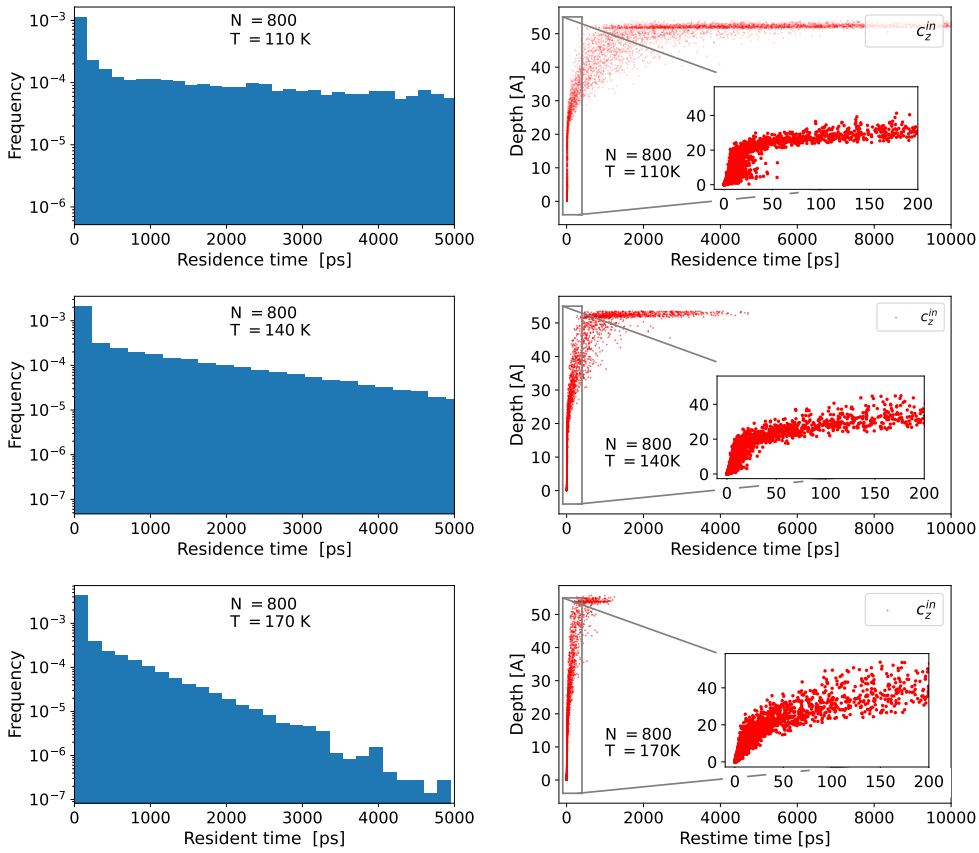

Figure 7: Left: Residence time distributions in logarithmic scale as a function of residence time. Right: Penetration depth as a function of residence time

phase, the bulk liquid (which has no layering structure) and the adsorbed layers, we can conclude that the time that the molecules spent in the latter is dominant. The data distributions also show three clear molecule motions and residence time regimes, gaseous phase (data localized near the origin), the bulk liquid (data scattered) and the adsorbed layers (data localized near the wall).

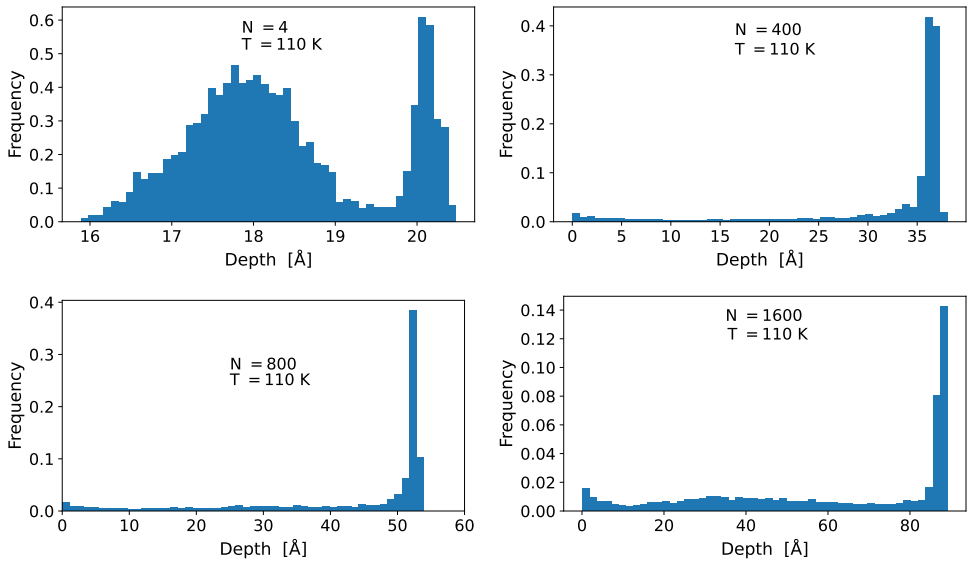

Figure 8: Penetration depth distributions at 110K.

Regarding the distributions of penetration depth in Figure 8, in all cases where a liquid film is present ($N \geq 400$), we find a peak corresponding to a location near the solid surface. This shows that a large number of molecules comes from that location and travels back to the gaseous phase. As the liquid film thickness increases, this peak decreases as more molecules come from inside the liquid bulk. Around the interface position at 20 Å, there is no clear dominant behavior, thus making it hard to use penetration depth to distinguish condensation molecules from penetration distribution. For the special case $N = 4$ where collisions are mostly between the gas molecules on the solid wall, the distribution reveals the roughness structure of the

silica wall. We can find two peaks at distance of 2 Å which correspond to the different local minima in silica where CH_4 molecules are most likely absorbed.

Let us focus on molecules with residence time shorter than 40 ps and molecules with penetration depth longer than 20 Å. From the depth distribution of short residence time molecules (see Fig. 9), we find that a significant portion of molecules penetrates farther than 20 Å and without exceeding 27 Å. On the other hand, looking at the distribution of residence time for short penetration depths, we find that most molecules stay a time shorter than 40 ps between the control plane and the solid wall.

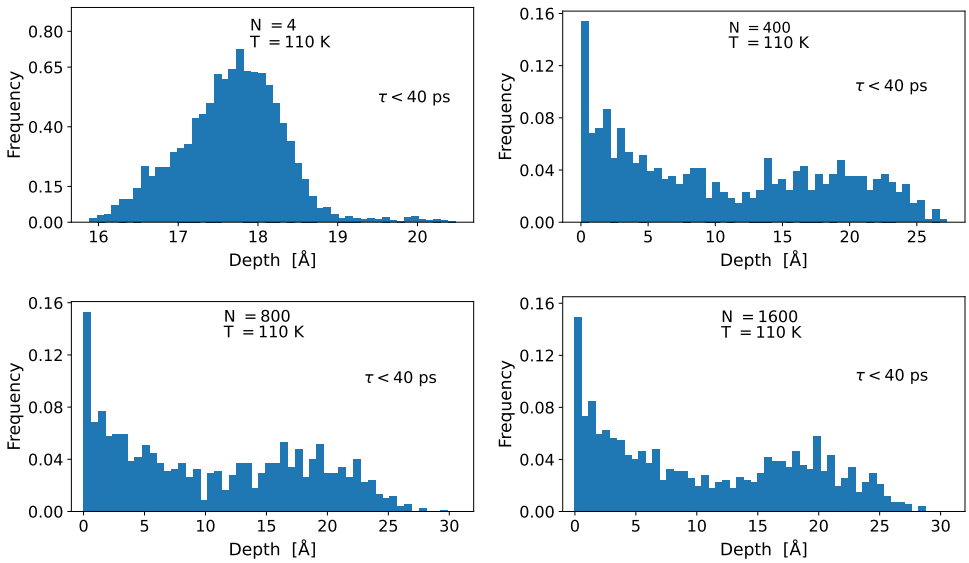

Figure 9: Penetration depth distributions for molecules with residence times shorter than 40 ps, and for different number of simulation molecules: $N = 4, 400, 800$ and 1600.

Similarly for the population with a penetration depth shorter than 20 Å, we can observe in Figure 10, the distribution of the residence time as a function of the number of methane molecules N. We can find that the number of molecules with residence time longer than 40 ps is very low. From the above observation, using penetration depths longer than 20 ps also guarantees the residence time to be longer than 40 ps but not vice versa.

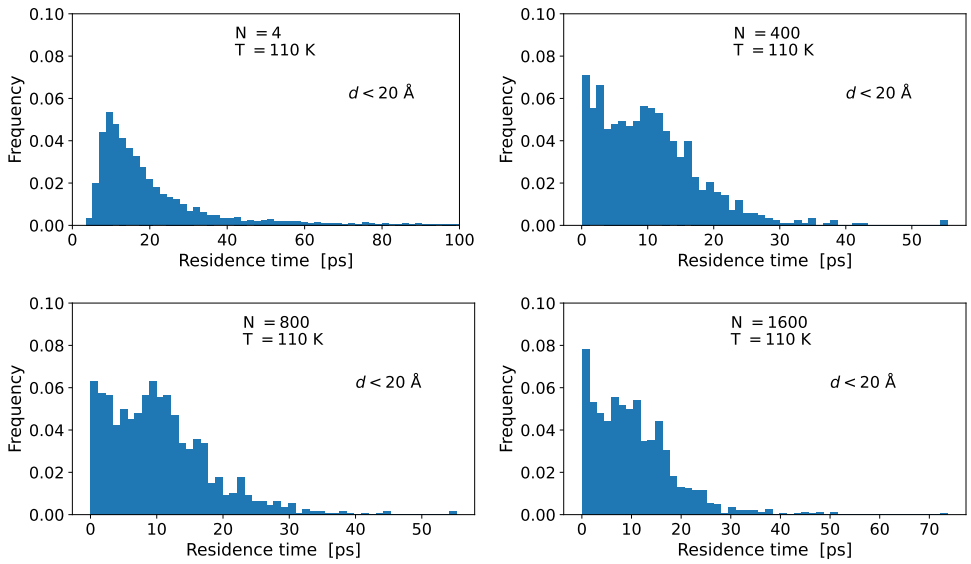

Figure 10: Residence time distribution for molecules with penetration depth shorter than 20 Å and for different number of simulation molecules: N =4, 400, 800 and 1600.

The above data distribution analysis shows us useful microscopic information of the atomic motion across the interface, especially how the long/short residence time is and how low/deep penetration depth is and also some explanation of their origins. We noted that the mass exchanges at the interface is complex and using the condensation coefficient is a simplification of the real condensation-reflection process as the differences between the condensation and reflected molecules are not very clear. The analysis suggests that using the penetration depth seems to provide a more coherent picture of the process. In the following, we introduce another tool based on correlation analysis which can allow calculating at the same time the condensation and the tangential momentum accommodation coefficients.

3.3. Evaporation/condensation and accommodation coefficients from correlation analysis

In this Section, we only focus on cases where the liquid film layer is formed and the use of condensation coefficient is meaningful. The early stage of the

condensation ($N = 4$) is no longer considered as it should be treated with adsorption physics instead.

For data analysis, let us denote the full data set $\mathcal{D}$ containing all the M events composed of the input velocity vector $\boldsymbol{c}'$, the output velocity vector $\boldsymbol{c}$, the residence time τ, and the penetration depth d recorded by the simulation

$$\mathcal{D} = \{\boldsymbol{X}^{(i)} | i = 1, ..., M\}, \quad \boldsymbol{X}^{(i)} = (\boldsymbol{c}'^{(i)}, \boldsymbol{c}^{(i)}, d^{(i)}, \tau^{(i)}). \tag{26}$$

We assume that the data set $\mathcal{D}$ can be divided into two subsets: $\mathcal{D}_{evap}$ for all evaporation events and $\mathcal{D}_{ref}$ for all reflection events. To study this, we denote the subsets according to residence time threshold, τ_c

$$\mathcal{D}_{\tau<\tau_c} = \{\boldsymbol{X}^{(i)} \in \mathcal{D} | \tau^{(i)} < \tau_c\}, \quad \mathcal{D}_{\tau>\tau_c} = \{\boldsymbol{X}^{(i)} \in \mathcal{D} | \tau^{(i)} > \tau_c\} \tag{27}$$

and penetration depth threshold, d_c

$$\mathcal{D}_{d<d_c} = \{\boldsymbol{X}^{(i)} \in \mathcal{D} | d^{(i)} < d_c\} \quad \mathcal{D}_{d>d_c} = \{\boldsymbol{X}^{(i)} \in \mathcal{D} | d^{(i)} > d_c\}. \tag{28}$$

Next $\rho_{Q,Q'|\mathcal{A}}$ is the correlation coefficient between $Q(\boldsymbol{c})$ and $Q'(\boldsymbol{c}')$, functions of velocity, for data belonging to data set $\mathcal{A}$

$$\rho_{Q',Q|\mathcal{A}} = \frac{cov(Q', Q)}{\sigma_Q \sigma_{Q'}} = \frac{\sum (Q - \langle Q \rangle)(Q' - \langle Q' \rangle)}{\sqrt{\sum (Q - \langle Q \rangle)^2 \sum (Q' - \langle Q' \rangle)^2}}. \tag{29}$$

We note that the incoming velocity $\boldsymbol{c}'^{(i)}$ is realization of $p^{in}(\boldsymbol{c}')$ and the outgoing $\boldsymbol{c}^{(i)}$ is realization of $p^{out}(\boldsymbol{c})$. We remark that for molecules staying longer and going deeper in the liquid phase, the outgoing velocity is less correlated with the incoming velocity. It is suggested that molecules which evaporate p^{evap} can be identified by a zero correlation, in agreement with Eq. (14).

First, we assume that the liquid surface is isotropic in the plane xOy. To improve the statistical signal, let us collect the two tangential velocity components c'_x and c'_y into one group c'_{xy} and c_x and c_y velocity components

into another group c_{xy} (see Fig. 11).

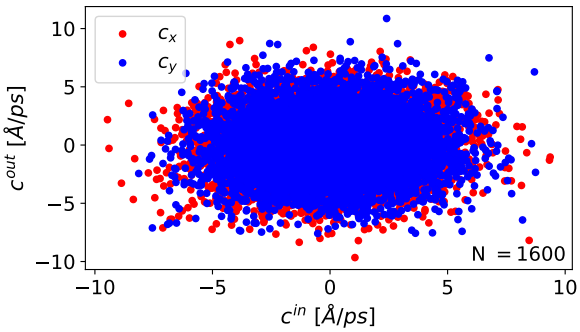

Figure 11: Data points of the input tangential velocities c'_x, c'_y and output tangential velocities c_x, c_y at 110K and $N = 1600$.

Next we compute the correlation coefficients between the quantities c'_{xy} and c_{xy} for a residence time τ less than τ_c or for a penetration depth d less than d_c, denoted shortly as

$$\rho^d_{xy}(d_c) = \rho_{c'_{xy},c_{xy}|\mathcal{D}_{d>d_c}}, \quad \rho^\tau_{xy}(\tau_c) = \rho_{c'_{xy},c_{xy}|\mathcal{D}_{\tau>\tau_c}}. \tag{30}$$

The evolution $\rho^d_{xy}(d_c)$ of the correlation coefficients as a function of the penetration depth threshold is given in Figure 12 for different temperatures and molecules numbers of methane. As expected, the correlation coefficient decreases with the penetration depth. For the case of $T = 110$K the correlation coefficient has a value of $0.05 - 0.06$ for small penetration depths and reaches a plateau at a value close to zero for penetration depths around $18 - 20$ Å. It is suggested using $18 - 20$ Å as threshold value for identifying an evaporated molecule, since a molecule outgoing through the control plane from this distance can be considered as independent of its initial state.

The same analysis can be made for the correlation coefficient $\rho^\tau_{xy}(\tau_c)$ in terms of residence time threshold. The correlation coefficient decreases with time τ_c and reaches a plateau after a certain residence time. This threshold value is about $20-40$ ps and seems to decrease as the film thickness decreases,

i.e N decreases from 1600 to 400.

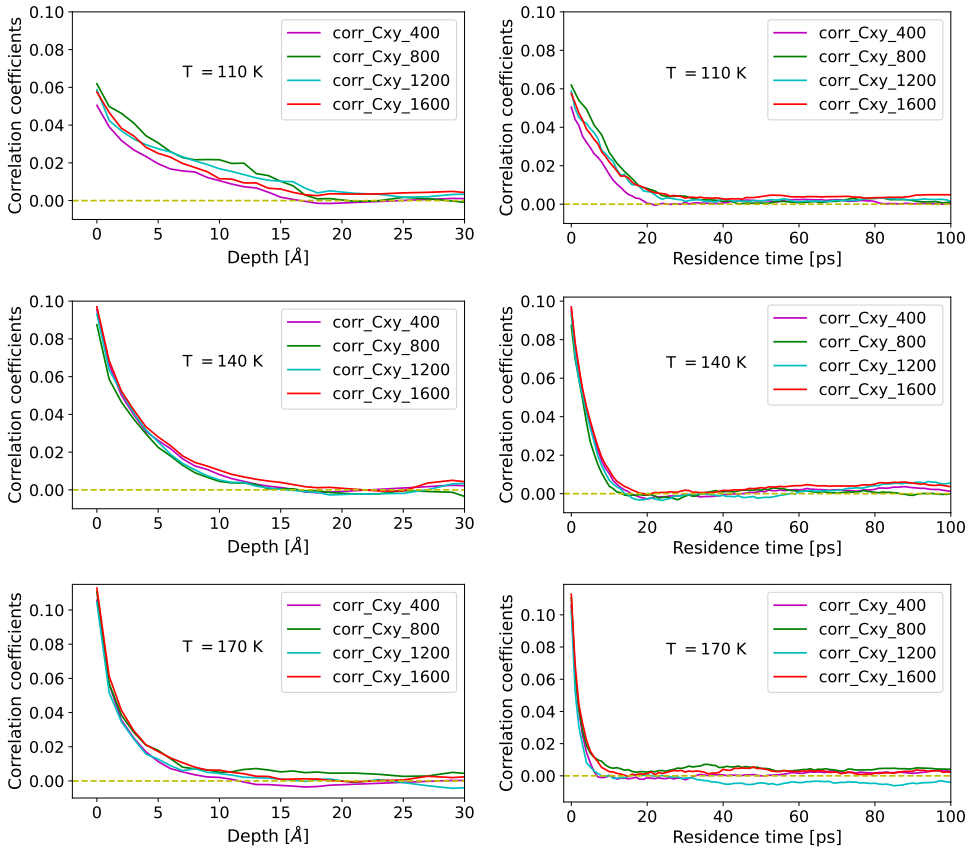

Figure 12: Evolution of the correlation coefficient of tangential velocity: left column, $\rho^{d}_{xy}(d_c)$ in terms of the penetration depth threshold d_c and right column, $\rho^{\tau}_{xy}(\tau_c)$ in terms of residence time threshold τ_c, for different temperatures and molecules numbers of methane.

From the correlation map shown in Fig. 13, we find a strong correlation between the velocity components of the same direction (c_x, c'_x), (c_y, c'_y) and (c_z, c'_z) at short residence time and penetration depth thresholds while the velocity components of different directions are uncorrelated. It suggests that the components of different directions are independent.

The analysis of the correlation coefficients provided above leads that the tangential momentum accommodation coefficient α and the condensation

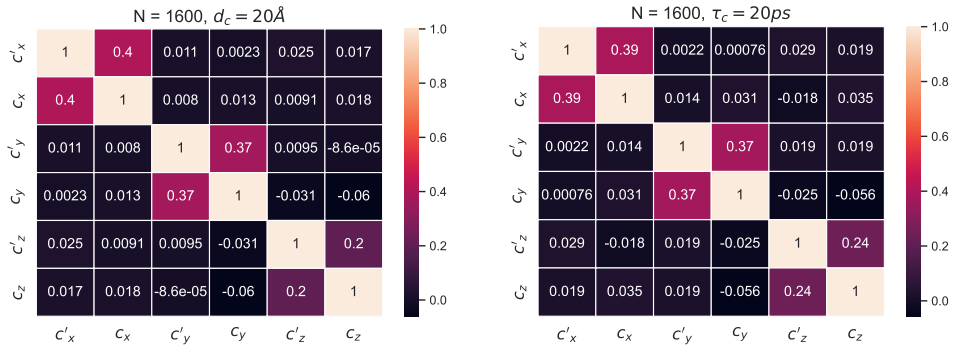

Figure 13: Correlation map between $\boldsymbol{c}$ (outgoing velocity) and $\boldsymbol{c}'$ (incoming velocity) for $\mathcal{D}_{d_c<20\mathring{A}}$ and $\mathcal{D}_{\tau_c<20ps}$. The color in the cell (a, b) where $a = c'_x, c'_y, c'_z$ and $b = c_x, c_y, c_z$ represents the value of correlation ρ_{ab} between a and b. The black and white colors represent the values 0 and 1 and other colors represent intermediate values. Values close to 1 means strong correlation and values close to 0 mean weak correlation.

coefficient α_c could be computed by the relations

$$\alpha_c = \frac{|\mathcal{D}_{evap}|}{|\mathcal{D}|}, \quad \alpha = 1 - \rho_{c'_{xy},c_{xy}|\mathcal{D}_{ref}}, \quad \mathcal{D}_{ref} = \mathcal{D}\backslash\mathcal{D}_{evap} \tag{31}$$

with $\mathcal{D}_{evap}$ being either $\mathcal{D}_{\tau>\tau_c}$ or $\mathcal{D}_{d>d_c}$, τ_c varying from $20-40$ ps and d_c varying from $18-20$ Å. The notation $||$ represents the data size or the number of elements of the data set. The last expression in (31) is due to $\mathcal{D} = \mathcal{D}_{ref} \cup \mathcal{D}_{evap}$ and the backward-slash $\backslash$ is the subtraction operation between the dataset. The distribution of $\boldsymbol{c}$ in $\mathcal{D}_{evap}$ is expected to follow the distribution p^{evap} and $\boldsymbol{c}, \boldsymbol{c}'$ in $\mathcal{D}$ follow p^{out},p^{in}, $\boldsymbol{c}, \boldsymbol{c}'$ in $\mathcal{D}_{ref}$ follow $p^{ref/out}$,$p^{ref/in}$. As a result, the correlation is connected to the accommodation coefficient according to the remarks in Section 2.1 and Appendix A

In each model consisting of N methane molecules, we define the thickness of the liquid film as the distance between the top surface of the quartz crystal and the liquid-gas interface. By varying τ_c (from 20 to 40 ps) and d_c (from 18 to 20 Å), see Fig. 14, we find that the condensation and the tangential momentum accommodation coefficients are almost insensible to the choice of

those parameters. The condensation coefficient lies in range $0.85 - 0.9$ and the tangential momentum accommodation coefficient between $0.52 - 0.67$. To the best of our knowledge, there is no previous experimental and simulation works on those coefficients for methane. We find that the condensation coefficient is in the same range as the literature works [9, 11, 13, 15] in equilibrium and non equilibrium cases on other fluids. But none of them have considered and computed the tangential momentum accommodation coefficient as done in this work. In Ref. [9], non equilibrium MD simulations of LJ fluid were done using reduced cutoff radius $r_{cut} = 2.5\sigma$ and the condensation and evaporation coefficients are found between 0.5-0.8. In Ref. [11], the authors used equilibrium MD simulations with $r_{cut} = 3.2\sigma$ and found the condensation and evaporation coefficients between 0.75-0.98. In Ref. [13], thin films are constituted of $n-$dodecanes, larger molecules with internal degree of freedom, and α_c ranges from 0.5-0.6. In Ref. [15], a liquid droplet is considered and α_c is found to be dependent on droplet curvature. The values for infinite radius are around 0.8 for LJ fluid but can be as small as 0.1-0.2 for water.

It is interesting to note that using $d_c = 20$ Å or $\tau_c = 20$ ps yields close coefficient values, situated in the middle of the ranges. Using $d_c = 18$ Å and $\tau_c = 40$ ps gives extreme values. As $d_c = 20$ Å has the physical meaning previously explained and using τ_c may omit atoms travelling near parallel to the interface, we shall adopt this criteria for the following analysis.

From Fig. 14, we also find that the condensation coefficient decreases slightly as the film thickness increases. It means that at the early stage of condensation, molecules tend to condense more and to reflect less. Only when the film reaches a certain thickness (around 90 Å), the coefficient starts to stabilize and becomes constant. Due to the influence of the film thickness and the presence of the solid substrate, the tangential momentum accommodation coefficient slightly varies but with a rather complex trend. In particular, we observe a local minimum at 30 Å thickness.

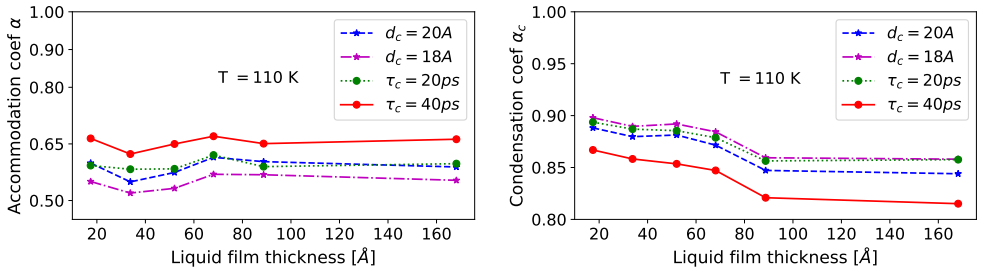

Figure 14: Variation of the tangential momentum accommodation coefficient α and condensation coefficient α_c with liquid film thickness.

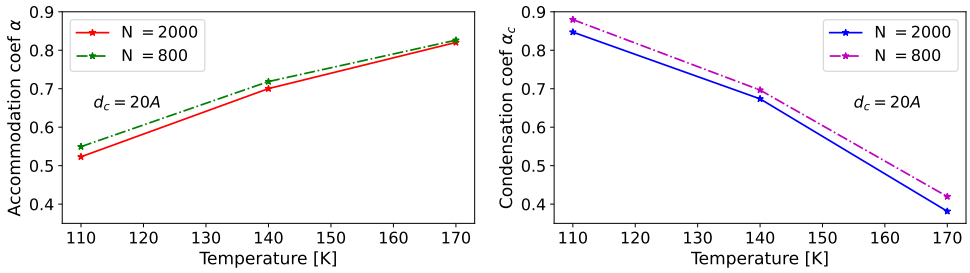

Figure 15: Variation of the tangential momentum accommodation coefficient α and condensation coefficient α_c with respect to temperature.

Finally, we examined the dependency of the two coefficients α and α_c with temperature. Fig. 15 shows that as the temperature increases from 110K to 170K, the condensation coefficient decreases and the tangential momentum accommodation coefficient increases with a variation of approximately 50% between the maximal and the minimal values. It is noted that at high temperature, the interface thickness is larger and the vapor phase is denser, making harder for molecules to cross and condense in the liquid phase. Molecules are more likely to collide with other molecules and to come back to the vapor, so α_c decreases. Regarding reflected atoms, thick interphase with high density also reduces the mean free path and increases the number of collisions and thus the reflected atoms velocity is more diffusive, less correlated and consequently leads to a high tangential velocity accommodation coefficient α.

	$T = 110$K		$T = 140$K		$T = 170$K	
N	α_c	α	α_c	α	α_c	α
400	0.89	0.60	0.70	0.69	0.45	0.80
800	0.88	0.55	0.70	0.72	0.42	0.83
1200	0.88	0.57	0.68	0.71	0.42	0.83
1600	0.87	0.61	0.70	0.69	0.39	0.83
2000	0.85	0.60	0.67	0.70	0.38	0.79
4000	0.84	0.59	0.64	0.72	0.41	0.79

Table 3: Condensation, α_c and tangential momentum accommodation, α, coefficients for different temperatures and different numbers of methane molecules N.

The summary of the condensation, α_c and tangential momentum accommodation, α, coefficients for different temperatures and different numbers of methane molecules N are provided in Table 3. The underlined above tendency of the condensation coefficient decreasing with increasing of temperature is clearly seen. Similar behaviour of deceasing of the condensation coefficient of mercury vapor with temperature rises was found by the authors of Ref. [18], where this coefficient was extracted from the experimental data. As it concerns the tangential momentum accommodation coefficient, we do not found any data on its sensitivity to the temperature, especially because this coefficient was extracted for gas-solid surface case and not for the case of reflected molecules from the liquid interface.

Quantitatively, we can reason that the velocity correlation coefficient of a particle after number N_{col} of independent collisions, $\gamma_{N_{col}}$, is equal to $\gamma_1^{N_{col}}$, where γ_1 is the velocity correlation coefficient after one collision. This coefficient is equal to 3/7 for hard sphere intermolecular potential [44]. As $\gamma_1 < 1$, the correlation decreases exponentially to 0 with the number of collisions N_{col} increasing. Since our transition layer has a finite size and is inhomogeneous, the number of collisions is not a constant for all molecules. To the first order of estimation, let us assume that the average number of collision N_{col} is of order l_c/λ with l_c being characteristic length of the transition layer and λ being the molecular mean free path. From Eq. (23), λ is inversely pro-

portional to the vapor number density and particularly to the characteristic interphase number density n_{int}, leading to the relation $N_{col} \propto l_c n_{int}$. As a result, $(1-\alpha) \propto \gamma_1^{l_c n_{int}}$ and $\ln(1-\alpha)$ is expected to be a linear function of the number density n_{int} with negative slope (due to $\ln \gamma_1 < 0$). Taking $n_{int} = 1/2(n_{sat}^{v} + n_{sat}^{liq})$ (Eq. (25)), and plotting its relation with the coefficient $\ln(1-\alpha)$ in Fig. 16, we find that a linear relation of type

$$\ln(1-\alpha) = An_{int} + B, \quad or, \quad \alpha = 1 - e^{An_{int}+B} \tag{32}$$

with $A = -404.38$ Å^3 and $B = 2.5255$, gives a good representation of the data in the temperature range $110 - 170$K.

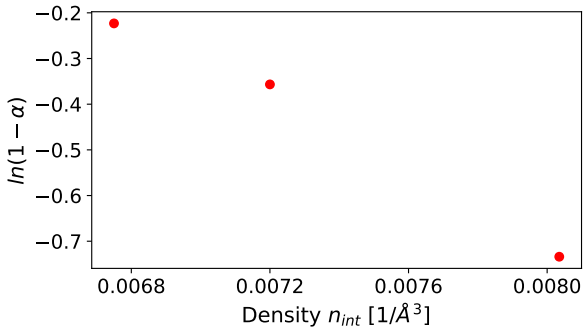

Figure 16: Relation between $\ln(1-\alpha)$ and n_{int}

4. Conclusions and perspectives

In this paper, we investigate the variation of number density, mass and momentum exchanges at the methane liquid vapor interface by Molecular Dynamics simulations. Information about residence time and penetration depth of each molecule crossing a control plane located 20 Å far from the interface, is collected and then analyzed. We show that by using correlation analysis, we can determine at the same time the condensation coefficient and tangential momentum accommodation coefficient. This approach is new and

has not been yet studied in literature works.

Regarding the saturated number density, the MD simulations based on a large cut off distance yield results closed to the experiments. We also find the dependency of those coefficients in terms of liquid film thickness and temperature. Especially, when temperature increases up to near the critical temperature of methane T_c =190 K, the condensation coefficient decreases and the momentum accommodation coefficient increases drastically, meaning molecules condense less and reflect more at the interface and the reflection is more diffusive. A physics based empirical formula for the accommodation coefficient depending on the interface number density is also proposed.

The present work provides tool to identify the condensation, evaporation and tangential momentum accommodation coefficients using equilibrium MD simulations by looking those processes at the microscopic (atomic) scale. In the next step, it is interesting to investigate non equilibrium systems and examine how the microscopic processes deviate from equilibrium. Many open questions will be addressed, for example the difference between condensation and evaporation coefficients, the relaxation difference between the normal and the tangential directions [45], the presence of non-condensable gas [41]. The information from the simulations constitutes numerical evidences to construct more accurate KBCs in the future.

Appendix A. Expressions for scattering kernels

Different scattering kernels can be used to determine the outgoing distribution function if the incident one is known as it is defined by Eq. (3). The expression of Maxwell scattering kernel is the following

$$B^M(\boldsymbol{c}|\boldsymbol{c}') = (1-\alpha)\delta(\boldsymbol{c}-\boldsymbol{c}'^s) + \alpha\sqrt{\frac{2\pi}{\theta_w}}|c_z|\mathcal{M}(\boldsymbol{c}) \qquad \text{(A.1)}$$

where δ is the delta dirac distribution and $\boldsymbol{c}'^s$ is the mirror counterpart of the incoming velocity $\boldsymbol{c}'$ like in Eq. (12).

For the Cercignani-Lampis scattering kernel this expression reads

$$B^{CL}(\boldsymbol{c}|\boldsymbol{c}') = \frac{e^{-\frac{(c_x-(1-\alpha)c'_x)^2+(c_y-(1-\alpha)c'_y)^2}{2\alpha(2-\alpha)\theta_w}}}{2\pi\theta_w\alpha(2-\alpha)} \frac{c_z e^{-\frac{c_z^2+(1-\alpha_n)c_z^2}{2\alpha_n\theta_w}}}{\alpha_n\theta_w} I_0\left(\frac{\sqrt{1-\alpha_n}c_z c'_z}{\alpha_n\theta_w}\right), \tag{A.2}$$

where $\theta_w = k_B T_w/m$ and I_0 is the modified Bessel function of first kind and zeroth order. Here α_n is the accommodation coefficient associated to the normal kinetic energy.

It is possible to show that the correlation parameters are connected to the accommodation coefficients α. Let us take the Cercignani-Lampis kernel for example. The function $B^{CL}(\boldsymbol{c}|\boldsymbol{c}')$ is the conditional probability function of reflected velocity $\boldsymbol{c}$ for given incoming velocity $\boldsymbol{c}'$. The joint probability $B^{CL}(\boldsymbol{c},\boldsymbol{c}')$ can be computed by

$$B(\boldsymbol{c},\boldsymbol{c}') = B(\boldsymbol{c}|\boldsymbol{c}')p^{in}(\boldsymbol{c}') \tag{A.3}$$

and the correlation parameters between the tangential velocities c_x, c'_x is

$$\rho_{c'_x c_x} = \frac{\int B(\boldsymbol{c},\boldsymbol{c}')c'_x c_x d\boldsymbol{c} d\boldsymbol{c}'}{\sqrt{\int (c_x)^2 p^{ref/out}(\boldsymbol{c})d\boldsymbol{c}}\sqrt{\int (c'_x)^2 p^{in}(\boldsymbol{c}')d\boldsymbol{c}'}} \tag{A.4}$$

In equilibrium, the incoming and the outcoming distributions $p^{ref/out}(\boldsymbol{c}')$ and $p^{in}(\boldsymbol{c})$ are identical to

$$p^{ref/out}(\boldsymbol{c}) = \sqrt{\frac{2\pi}{\theta_w}}|c_z|\mathcal{M}(\boldsymbol{c}), \quad p^{in}(\boldsymbol{c}') = \sqrt{\frac{2\pi}{\theta_w}}|c'_z|\mathcal{M}(\boldsymbol{c}') \tag{A.5}$$

and

$$B^{CL}(\boldsymbol{c},\boldsymbol{c}') = \frac{e^{-\frac{(c_x^2-2(1-\alpha)c_x c_x'+c_x'^2)}{2\alpha(2-\alpha)\theta_w}}}{2\pi\theta_w\sqrt{\alpha(2-\alpha)}}\frac{e^{-\frac{(c_y^2-2(1-\alpha)c_y c_y'+c_y'^2)}{2\alpha(2-\alpha)\theta_w}}}{2\pi\theta_w\sqrt{\alpha(2-\alpha)}}\frac{|c_z c_z'|e^{-\frac{(c_z^2+c_z'^2)}{2\alpha_n\theta_w}}}{\alpha_n\theta_w^2}\times$$
$$I_0\left(\frac{\sqrt{1-\alpha_n}c_z c_z'}{\alpha_n\theta_w}\right) \tag{A.6}$$

This corresponds in fact to two independent bivariate Gaussian for c_x, c_x' and c_y, c_y' with the same correlation $1-\alpha$ multiplied with a special distribution of c_z, c_z' (Bessel and exponential). Using A.4, A.5, A.6, we can show that $\rho_{c_x' c_x} = 1-\alpha$.

Regarding the Maxwell kernel, at equilibrium we have

$$B^M(\boldsymbol{c},\boldsymbol{c}') = (1-\alpha)\delta(\boldsymbol{c}-\boldsymbol{c}'^s)\sqrt{\frac{2\pi}{\theta_w}}|c_z|\mathcal{M}(\boldsymbol{c}') + \alpha\frac{2\pi}{\theta_w}|c_z c_z'|\mathcal{M}(\boldsymbol{c})\mathcal{M}(\boldsymbol{c}') \tag{A.7}$$

Due to the fact that the second term gives zero c_x, c_x' correlation, we have

$$\int B^M(\boldsymbol{c},\boldsymbol{c}')c_x c_x' d\boldsymbol{c}d\boldsymbol{c}' = (1-\alpha)\int \delta(\boldsymbol{c}-\boldsymbol{c}'^s)c_x c_x'\sqrt{\frac{2\pi}{\theta_w}}|c_z|\mathcal{M}(\boldsymbol{c}')d\boldsymbol{c}d\boldsymbol{c}'$$
$$= (1-\alpha)\int c_x^2\sqrt{\frac{2\pi}{\theta_w}}|c_z|\mathcal{M}(\boldsymbol{c})d\boldsymbol{c} \tag{A.8}$$

Again substituting this result into A.4, A.5, A.7, we can show that $\rho_{c_x' c_x} = 1-\alpha$

Appendix B. Expression for saturation number density of methane

From experimental data and equation of state (EOS) for methane [35]

$$\ln\frac{\rho_{sat}^v}{\rho_c} = \sum_{i=1}^{6} a_i\left(1-\frac{T}{T_c}\right)^{p_i}, \quad \rho_{sat}^v = n_{sat}^v m_{CH_4} \tag{B.1}$$

with

$$
\begin{aligned}
&a_1 = -1.8802840, \quad a_2 = -2.8526531, \quad a_3 = -3.0006480, \\
&a_4 = -5.2511690, \quad a_5 = -13.191859, \quad a_6 = -37.553961 \\
&p_1 = 0.354, \quad p_2 = 5/6, \quad p_3 = 3/2, \\
&p_4 = 5/2, \quad p_5 = 25/6, \quad p_6 = 47/6,
\end{aligned} \tag{B.2}
$$

and $T_c = 190.564$K and $\rho_c = 162.66$ kg/m^3.

Nomenclature

Abbreviations and Sets

$\mathcal{D}$ full analysis data set, containing velocity, penetration depth, and residence time for all particles

$\mathcal{D}_{evap}$ subset of the dataset $\mathcal{D}$ for all evaporation events

$\mathcal{D}_{ref}$ subset of the data set $\mathcal{D}$ for all reflection events

BKS force field for silica proposed by Besst, Kamer, and Santen

KBC Kinetic Boundary Condition

LJ Lennard-Jones

MC Monte Carlo

MD Molecular Dynamics

PDD Penetration Depth Distribution

RTD Residence Time Distribution

Other symbols

α momentum/energy accommodation coefficient

α_c condensation coefficient

α_e evaporation coefficient

α_n accommodation parameter of the normal energy component

α_t accommodation parameter of the tangential momentum

$\boldsymbol{c}'$ incoming velocity of the gas phase at the interface

$\boldsymbol{c}$ outgoing velocity of the gas phase at the interface

$\boldsymbol{c}^s$ mirror velocity of $\boldsymbol{c}$ with respect to the interface normal to $\widehat{\boldsymbol{i}}_z$

$\mathcal{M}$ Maxwell-Boltzmann distribution (or the Maxwellian)

δ distance between the control plane and the liquid-vapor interface

ϵ_{ij} depth of potential well or dispersion energy

γ_n velocity correlation coefficient after n independent collisions

λ molecular mean free path of methane vapor

ρ_x^d evolution of correlation coefficients for the velocity component x

ρ_x^τ evolution of correlation coefficients for the velocity component x

$\rho_{Q,Q'/\mathcal{A}}$ correlation coefficient between $Q(\boldsymbol{c})$ and $Q'(\boldsymbol{c}')$, functions of velocity, for data belonging to data set $\mathcal{A}$

σ_{ij} distance at which the particle-particle potential energy V_{ij}^{LJ}

τ residence time of the gas particle as it crosses the control plane from the gas phase to the liquid phase and back to the gas phase

τ_c residence time threshold

$B(\boldsymbol{c}/\boldsymbol{c}')$ scattering kernel relating the distribution of incoming and outgoing particles

C energy conversion constant for the Coulombic term

d penetration depth of the gas particle from the control plane into the liquid phase

d_c penetration depth threshold

f^{in} distribution function of incoming gas particles at a interface

f^{out} distribution function of outgoing gas particles at a interface

l_c characteristic length of the transition layer between the vapor-liquid phase

m mass of the fluid molecule

N number of methane molecules in the system

n vapor number density

N_{col} number of independent collisions of a particle

n_{int} number density at the boundary between the liquid and vapor phases

n_{sat}^{liq} saturated liquid number density

n_{sat}^{v} saturated vapor number density

n_w gas number density at the interface at temperature T_w

p^a normalized probability distribution function associated with the flux crossing the interface

q_i coulombic charges of the atoms i

r_{cut} cutoff distance for force computation

r_{ij} distance between atoms i and j

T system temperature at equilibrium

T_c critical point temperature

T_{tp} triple point temperature

T_w Temperature of the solid wall (quartz substrate)

V_{ij}^{BKS} pair potential between two atoms j and i according to the BKS model

V_{ij}^{LJ} pair potential between two atoms j and i according to the Lennard-Jones (LJ) model

X^* Reduced state parameters X in Lennard-Jones units

Physics constants

k_B Boltzmann constant

References

[1] M. Knudsen, Die maximale verdampfungsgeschwindigkeit des quecksilbers, Ann. Phys. 352 (1915) 697–708.

[2] Y. B. Zudin, Non-equilibrium evaporation and condensation processes, Springer, 2019.

[3] H. Hertz, Ueber die verdunstung der flüssigkeiten, insbesondere des quecksilbers, im luftleeren raume, Ann. Phys. 253 (1882) 177–193.

[4] R. W. Schrage, A theoretical study of interphase mass transfer, in: A Theoretical Study of Interphase Mass Transfer, Columbia University Press, 1953.

[5] V. P. Carey, Statistical thermodynamics and microscale thermophysics, Cambridge University Press, 1999.

[6] S. I. Anisimov, Vaporization of metal absorbing laser radiation, Journal of Experimental and Theoretical Physics 54 (1968) 339–342.

[7] T. Ytrehus, Molecular flow effects in evaporation and condensation at interfaces, Multiphase Sci. Technol. 9 (1997).

[8] R. Marek, J. Straub, Analysis of the evaporation coefficient and the condensation coefficient of water, Int. J. Heat Mass Transf. 44 (2001) 39–53.

[9] R. Meland, A. Frezzotti, T. Ytrehus, B. Hafskjold, Nonequilibrium molecular-dynamics simulation of net evaporation and net condensation, and evaluation of the gas-kinetic boundary condition at the interphase, Phys. Fluids. 16 (2004) 223–243.

[10] T. Ishiyama, T. Yano, S. Fujikawa, Molecular dynamics study of kinetic boundary condition at an interface between argon vapor and its condensed phase, Phys. Fluids 16 (2004) 2899–2906.

[11] Z. Liang, T. Biben, P. Keblinski, Molecular simulation of steady-state evaporation and condensation: Validity of the schrage relationships, Int. J. Heat Mass Transf. 114 (2017) 105–114.

[12] T. Tsuruta, H. Tanaka, T. Masuoka, Condensation/evaporation coefficient and velocity distributions at liquid–vapor interface, Int. J. Heat Mass Transf. 42 (1999) 4107–4116.

[13] B.-Y. Cao, J.-F. Xie, S. S. Sazhin, Molecular dynamics study on evaporation and condensation of n-dodecane at liquid–vapor phase equilibria, J. Chem. Phys. 134 (2011) 164309.

[14] G. Nagayama, M. Takematsu, H. Mizuguchi, T. Tsuruta, Molecular dynamics study on condensation/evaporation coefficients of chain molecules at liquid–vapor interface, J. Chem. Phys. 143 (2015) 014706.

[15] P. L. Barclay, J. R. Lukes, Curvature dependence of the mass accommodation coefficient, Langmuir 35 (2019) 6196–6202.

[16] A. Chandra, P. Keblinski, Investigating the validity of schrage relationships for water using molecular dynamics simulations, J. Chem. Phys. 153 (2020) 124505.

[17] I. A. Graur, E. Y. Gatapova, M. Wolf, M. A. Batueva, Non-equilibrium evaporation: 1d benchmark problem for single gas, Int. J. Heat Mass Transf. 181 (2021) 121997.

[18] I. A. Graur, M. A. Batueva, M. Wolf, E. Y. Gatapova, Non-equilibrium condensation, Int. J. Heat Mass Transf. 198 (2022) 123391.

[19] H. Struchtrup, A. Beckmann, A. S. Rana, A. Frezzotti, Evaporation boundary conditions for the r13 equations of rarefied gas dynamics, Phys. Fluids 29 (2017) 092004.

[20] M. Liao, R. Grenier, Q.-D. To, M. P. de Lara-Castells, C. Léonard, Helium and argon interactions with gold surfaces: Ab initio-assisted determination of the he–au pairwise potential and its application to accommodation coefficient determination, J. Phys. Chem. 122 (2018) 14606–14614.

[21] M. Liao, Q.-D. To, C. Léonard, V. Monchiet, Non-parametric wall model and methods of identifying boundary conditions for moments in gas flow equations, Phys. Fluids 30 (2018) 032008.

[22] M. Voltolini, H. Wenk, N. Mondol, K. Bjørlykke, J. Jahren, Anisotropy of experimentally compressed kaolinite-illite-quartz mixtures, Geophysics 74 (2009) D13–D23.

[23] S. Tian, V. Erastova, S. Lu, H. Greenwell, T. Underwood, H. Xue, F. Zeng, G. Chen, C. Wu, R. Zhao, Understanding model crude oil component interactions on kaolinite silicate and aluminol surfaces: Toward improved understanding of shale oil recovery, Energy and Fuels 32 (2018) 1155–1165.

[24] A. T. Onawole, M. S. Nasser, I. A. Hussein, M. J. Al-Marri, S. Aparicio, Theoretical studies of methane adsorption on silica-kaolinite interface for shale reservoir application, Applied Surface Science 546 (2021) 149164.

[25] V. D. Chari, P. S. Prasad, S. R. Murthy, Hollow silica: A novel material for methane storage, Oil Gas Science and Technology – Rev. IFP Energies nouvelles 70 (2015) 1125–1132.

[26] M. G. Martin, J. I. Siepmann, Transferable potentials for phase equilibria. 1. united-atom description of n-alkanes, J. Phys. Chem. B 102 (1998) 2569–2577.

[27] Y. Sone, Kinetic theory and fluid dynamics, Springer, 2002.

[28] C. Cercignani, Mathematical methods in kinetic theory, Premuim Press, New York, London, 1990.

[29] T. T. Pham, Q. D. To, G. Lauriat, C. Léonard, V. Van Hoang, Effects of surface morphology and anisotropy on the tangential-momentum accommodation coefficient between Pt (100) and Ar, Phys. Rev. E 86 (2012) 051201.

[30] P. Spijker, A. J. Markvoort, S. V. Nedea, P. A. Hilbers, Computation of accommodation coefficients and the use of velocity correlation profiles in molecular dynamics simulations, Phys. Rev. E 81 (2010) 011203.

[31] M. Liao, Q.-D. To, C. Léonard, W. Yang, Prediction of thermal conductance and friction coefficients at a solid-gas interface from statistical learning of collisions, Phys. Rev. E 98 (2018) 042104.

[32] V. Beest, Kramer, Force field for silicas and aluminophosphates based on ab initio calculations, Phys. Rev. Lett. (1990) 2–3.

[33] R. T. Cygan, J.-J. Liang, A. G. Kalinichev, Molecular models of hydroxide, oxyhydroxide, and clay phases and the development of a general force field, J. Phys. Chem. B 108 (2004) 1255–1266.

[34] D. Frenkel, B. Smit, Understanding molecular simulation: from algorithms to applications, volume 1, Elsevier, 2001.

[35] U. Setzmann, W. Wagner, A new equation of state and tables of thermodynamic properties for methane covering the range from the melting line to 625 k at pressures up to 100 mpa, J. Phys. Chem. Ref. Data 20 (1991) 1061–1155.

[36] A. P. Thompson, H. M. Aktulga, R. Berger, D. S. Bolintineanu, W. M. Brown, P. S. Crozier, P. J. in't Veld, A. Kohlmeyer, S. G. Moore, T. D. Nguyen, et al., Lammps-a flexible simulation tool for particle-based materials modeling at the atomic, meso, and continuum scales, Comput. Phys. Commun. 271 (2022) 108171.

[37] J.-P. Hansen, I. R. McDonald, Theory of simple liquids, Academic press, 2006.

[38] J. Vrabec, G. K. Kedia, G. Fuchs, H. Hasse, Comprehensive study of the vapour–liquid coexistence of the truncated and shifted lennard–jones fluid including planar and spherical interface properties, Mol. Phys. 104 (2006) 1509–1527.

[39] J. R. Errington, Direct calculation of liquid–vapor phase equilibria from transition matrix monte carlo simulation, J. Chem. Phy. 118 (2003) 9915–9925.

[40] S. Stephan, M. Thol, J. Vrabec, H. Hasse, Thermophysical properties of the lennard-jones fluid: Database and data assessment, J. Chem. Inf. Model. 59 (2019) 4248–4265.

[41] K. Ohashi, K. Kobayashi, H. Fujii, M. Watanabe, Evaporation coefficient and condensation coefficient of vapor under high gas pressure conditions, Scientific Reports 10 (2020) 8143.

[42] K. Ohashi, K. Kobayashi, H. Fujii, M. Watanabe, Mean-field kinetic theory analysis of vapor flow between evaporating and condensing interfaces in the presence of non-condensable gas molecules, Phys. Fluids 33 (2021).

[43] K. Ohashi, K. Kobayashi, H. Fujii, M. Watanabe, Vapor condensation induced by fast-moving liquid film in the presence of noncondensable gas molecules, Int. Commun. Heat Mass Transf. 142 (2023) 106622.

[44] F. Nakai, Y. Masubuchi, T. Uneyama, Short-time dynamics of a tracer in an ideal gas, Phys. Rev. E 102 (2020) 032104.

[45] T. Ishiyama, T. Yano, S. Fujikawa, Kinetic boundary condition at a vapor-liquid interface, Phys. Rev. Lett. 95 (2005) 084504.